Scripta Materialia 193 (2021) 22–26

Contents lists available at ScienceDirect

Scripta Materialia

journal homepage: www.elsevier.com/locate/scriptamat

The source of lattice rotation in rotating lattice single (RLS) crystals

Evan J. Musterman[a], Dmytro Savytskii[a], Volkmar Dierolf[b], Himanshu Jain[a,*]

[a] Materials Science and Engineering Department, Lehigh University, 5 East Packer Avenue, Bethlehem, PA 18015, USA
[b] Physics Department, Lehigh University, 16 Memorial Drive East, Bethlehem, PA 18015, USA

ARTICLE INFO

Article history:
Received 24 August 2020
Accepted 12 October 2020

Keywords:
Crystallization
Chalcogenide glass
Laser heating
Transmission electron microscopy
Dislocations

ABSTRACT

Laser heating can be used to produce single crystal architectures in glass with a lattice that rotates at a constant rate. Such metamaterials can offer properties that are disallowed by conventional crystal structures. To establish the mechanism of this lattice rotation, we used transmission electron microscopy (TEM) to directly observe and characterize dislocations in Sb_2S_3 crystal lines fabricated in Sb-S-I glass as a model system. The lattice rotation calculated from the density and Burgers vectors of edge dislocations agrees with lattice rotation values experimentally determined by electron backscatter diffraction (EBSD) and selected area diffraction patterns (SADP). These results provide the first direct proof of the dislocation mechanism of lattice rotation in rotating lattice single (RLS) crystals, and very likely other forms of growth actuated bending, twisting and noncrystallographic branching as seen in spherulites.

Rotating lattice single (RLS) crystal architecture in glass is a novel class of metamaterials, wherein the orientation of crystal lattice changes at a constant rate along its length [1]. The axis of rotation is determined by the dynamic temperature profile provided by laser scanning used during crystal growth, whereas the rate of rotation, Θ measured in $^\circ/\mu$m, depends on the orientation of the lattice relative to the growth direction, and can be modified by varying the laser characteristics [2,3]. Accordingly, it has become possible to engineer the fundamental lattice of a crystal, thereby offering the opportunity to introduce novel properties, such as optical chirality; locally varying refractive index; cross-effects that require lower crystal symmetry; etc. Obviously, the ability to realize such properties requires a detailed understanding of the structure of RLS crystals on the atomic scale. This understanding of the structure of rotating lattices should also be useful in resolving the debate on the mechanism behind the growth of spherulites that have been known for over a century to form under certain crystal growth conditions [4]. Their lattices are distorted to produce characteristic spherulitic morphologies depending on local conditions at the growth front [5], leading to their unusual properties. There are, however, important differences between RLS crystal and spherulite crystal growth. At high laser scanning speeds, the lattice of the former is well controlled and can be engineered to a well-defined rotation rate, whereas spherulites, like crystals grown at lower scanning speeds approaching isothermal conditions, the lattice formation is uncontrolled and usually comprises variable distortions [3]. Furthermore, RLS crystals can be grown to essentially unlimited lengths suitable for practical applications, whereas spherulites with fractal structures have remained largely a curiosity of crystal growth found in nature.

To establish the atomic scale structure of RLS crystals, electron backscatter diffraction (EBSD) maps were obtained that helped quantify Θ. Further, microscanning X-ray diffraction (μSXRD) analysis revealed the resemblance of the Laue patterns of RLS crystals to that of a plastically bent single crystal comprising of complex dislocation structure [1,6]. It would then appear plausible that the observed rotation of lattice of RLS crystals is simply a manifestation of similar dislocation structure, specifically, a random and/or aligned distribution of edge dislocations of the same sign [7,8]. However, note that the RLS crystals are not subjected to, at least intentionally, any plastic deformation, and do not show any macroscopic bending of shape relative to the surrounding glass. Therefore, the dislocation-based description of their structure remains a hypothesis needing validation. Direct observation of dislocations is also needed to establish the relative contribution to lattice rotation from other sources such as elastic strain gradients [9], subgrain boundaries [6], etc. Interestingly, lattice rotations have also been observed in transrotational crystals, albeit on much smaller length scales, where presence of dislocations is not energetically favorable [10,11]. The present work was motivated by these considerations, specifically to establish the role of dislocations in producing systematic, macroscopic rotation/distortion of the lattice. Here we report the first direct evidence of dislocation structure using

* Corresponding author at: Sinclair Lab 120A, 7 Asa Drive, Bethlehem, PA 18015, USA
E-mail addresses: dmytrosavytskii@yahoo.com (D. Savytskii), h.jain@lehigh.edu (H. Jain).

https://doi.org/10.1016/j.scriptamat.2020.10.027
1359-6462/

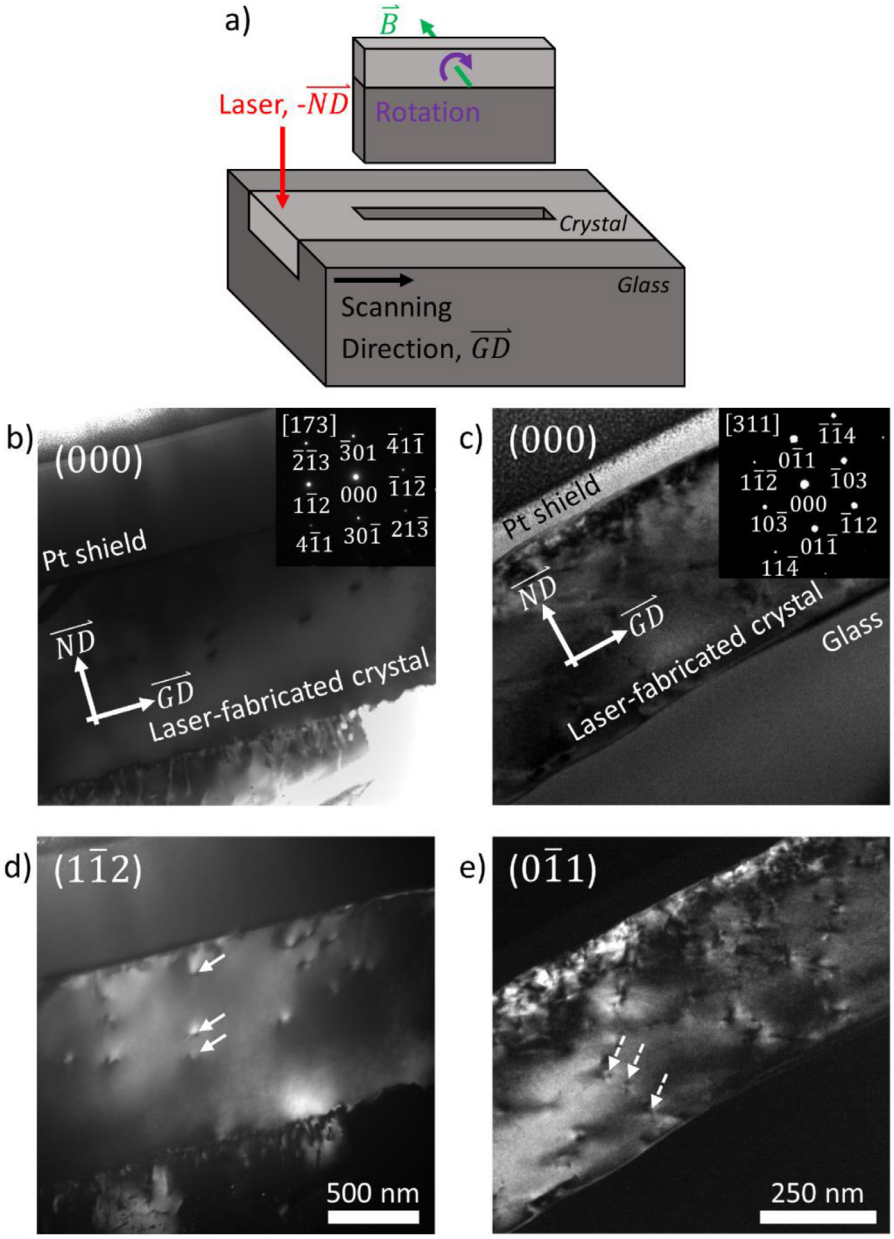

Fig. 1. Bright-field and selected dark-field images highlighting dislocations along laser-fabricated cross section. a) Schematic of TEM sample preparation. b) Bright-field image of crystal A with 0.11°/μm EBSD-measured rotation rate with normal ($\overrightarrow{ND}$) and growth direction ($\overrightarrow{GD}$) and labeled regions. Diffraction pattern insert of [173] direction. c) Bright-field image of crystal B with 0.29°/μm EBSD-measured rotation rate. Diffraction pattern insert of [311] direction. d) (1$\bar{1}$2) dark-field image of b and e) (0$\bar{1}$1) dark-field image of c. Solid arrows denote $^1/_2$[100] dislocations and dashed arrows denote $-^1/_4[\bar{1}02]$ dislocations.

transmission electron microscopy (TEM) of a model system: Sb_2S_3 RLS crystal lines fabricated by continuous wave (CW) laser in Sb-S-I glasses. We used dark-field TEM to image individual dislocations by relying on their lattice distortion.

A $16SbI_3$–$84Sb_2S_3$ model glass was fabricated according to the ampule quench method described previously [12] and polished with progressively finer abrasives finishing with 50 nm colloidal silica. Orthorhombic Sb_2S_3 crystal (a = 11.314 Å, b = 3.837 Å, c = 11.234 Å) [13] lines were fabricated by laser heating with a 639 nm continuous wave diode laser (LP637-SF70, ThorLabs) focused through a 50 × 0.75 NA objective lens with intensity ~100-150 $\mu W/\mu m^2$. TEM samples were prepared by extracting longitudinal cross sections (Fig. 1.a) from the laser-fabricated crystal lines using a focused ion beam (FEI Scios FIB), with the axis of crystal rotation parallel to the TEM electron beam, $\vec{B}$. Bulk crystal lines were analyzed in a scanning electron microscope (SEM, Hitachi 4300 SE) under low vacuum (~ 30-45 Pa) conditions. EBSD patterns were analyzed to yield lattice rotation rates with the TSL (TexSEM Laboratory) collection and analysis software [14]. TEM sample rotation was measured by selected area diffraction patterns (SADP) taken along the TEM sample length. Dislocations were characterized inside the TEM at 120 kV (JEOL 1200EX) and 200 kV (JEOL 2100) by observing lattice strain via diffraction from various sets of planes.

TEM dislocation analysis was performed on longitudinal cross-section samples (Fig. 1.a). Previous analysis on independent Sb_2S_3 crystals [15] showed only three possible dislocation slip systems ($^1/_2$[100], $^1/_4$[102], and $^1/_4[\bar{1}02]$). Using this knowledge, dislocations were identified for two laser-fabricated Sb_2S_3 crystal lines (crystals A and B) with Θ = 0.11°/μm and 0.29°/μm rotation rates measured by EBSD, respectively. Bright- and dark-field TEM images

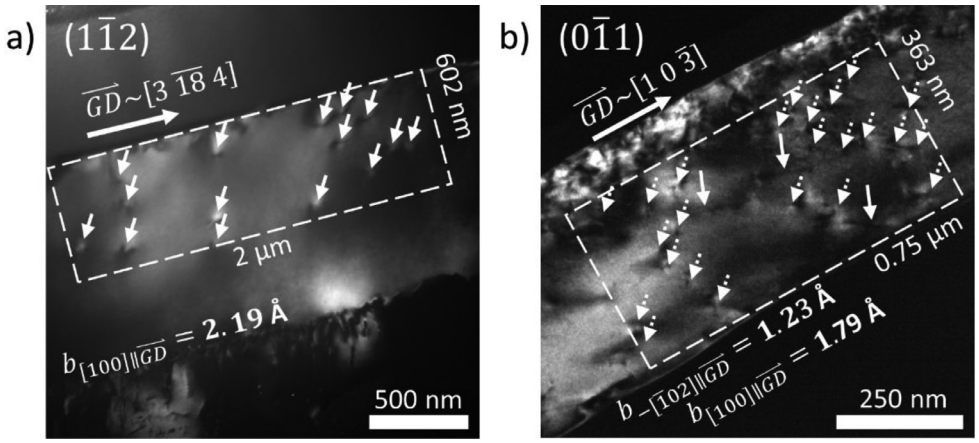

Fig. 2. Regions of crystals used for lattice rotation rate calculation. a) (1$\bar{1}$2) dark-field image from Fig. 1.**c.** b) (0$\bar{1}$1) dark-field image from Fig. 1.**d**. Both images show region and all enclosed dislocations marked for rotation calculation, solid arrows for $^1/_2$[100] and dashed arrows for $-^1/_4$[$\bar{1}$02]. Approximate $\overrightarrow{GD}$ and the Burgers vector component along $\overrightarrow{GD}$, are also indicated.

are shown for the two crystals (Fig. 1), where all images are oriented with growth direction ($\overrightarrow{GD}$) to the right and normal direction ($\overrightarrow{ND}$) up, opposite the laser propagation. Crystals were tilted towards the nearest zone axis, and their orientation ($\vec{B}$, $\overrightarrow{GD}$, and $\overrightarrow{ND}$) was determined from the SADP. Similar to Zhang et al. [16], dislocations were characterized geometrically by the minimum Burgers vector component along $\vec{B}$ and greatest Burgers vector component along $\overrightarrow{GD}$. These two requirements tend to minimize total dislocation energy by reducing the dislocation length required to transverse the crystal and minimizing the required dislocation density for rotation. Both samples included $^1/_2$[100] dislocations, whereas $-^1/_4$[$\bar{1}$02] dislocations were present in crystal B only (Fig. 1.d).

Lattice rotation can also be measured in the TEM by direct rotation of SADP and estimated by the dislocation density. SADP-measured crystal rotation was too small to measure for crystal A, but was 0.69°/μm for crystal B, more than double the EBSD-measured value. Arrays of dislocations can contribute rotation such as wedge (tilt boundary) and twist disclinations in the Volterra definition [17]. The rotation angle, θ, of a wedge disclination is given by $\theta \approx b/D$, where b is the magnitude of the Burgers vector and D is the spacing between edge dislocations as determined by Burgers [7]. The relation was generalized into three dimensions by Nye as $\Theta = b_{\overrightarrow{GD}}\,\rho_{\vec{B}}$ where $b_{\overrightarrow{GD}}$ is the Burgers vector component along $\overrightarrow{GD}$ and $\rho_{\vec{B}}$ is the dislocation density in the TEM image plane [8]. Using Nye's relation, lattice rotation rates were calculated for both crystal samples (Fig. 2), where $^1/_2$[100] and $-^1/_4$[$\bar{1}$02] are denoted by solid and dashed arrows, respectively. The dislocation density for crystal B was only measured for the lower portion of the crystal where dislocations were distinguishable due to non-interacting strain fields. Values of Θ were calculated as the sums of all dislocation angular contributions and are 0.16°/μm and 0.73°/μm for crystals A and B, respectively. For convenience, lattice rotation rates estimated by all three methods and approximate crystal directions are summarized in Table 1.

Based on μSXRD results, Savytskii et al. proposed that dislocations may form as part of the crystal growth process under the confinement of highly viscous glass [1]. Stresses are generated at the crystal-glass interface as a result of the smaller molar volume of the crystal than the glass matrix. As predicted by them, edge dislocations are observed within both RLS crystals, and their orientation within the sample is highly aligned, supporting the presence of a well-defined externally imposed cause, rather than some random fluctuation of the crystal growth process. The Burgers vectors

Table 1
Lattice rotation rates and approximate crystal directions.

	Crystal A	Crystal B
Rotation rate Θ		
by EBSD	0.11°/μm	0.29°/μm
by SADP	-	0.69°/μm
by dislocation density	0.16°/μm	0.73°/μm
Direction		
$\overrightarrow{GD}$	[3 $\bar{1}$8 4]	[1 0 $\bar{3}$]
$\overrightarrow{ND}$	[10 6 $\bar{5}$]	[2 $\bar{5}$6 1]
$\vec{B}$	[1 7 3]	[3 1 1]

of these dislocations tend to be parallel to $\overrightarrow{GD}$ and perpendicular to the axis of rotation, $\vec{B}$. The distribution of dislocations, as seen in Fig. 2, is mostly random along $\overrightarrow{GD}$ with some alignment in the perpendicular direction, tending towards the formation of small-angle tilt boundaries (polygonization) that may become more prominent given greater dislocation mobility. There is a nonuniform local dislocation density distribution with dislocations concentrated near the top of the crystals. The upper crystal region would have experienced the greatest temperatures and stresses during crystallization, both of which would contribute to higher dislocation density.

Lattice rotation rates measured experimentally and calculated based on average dislocation density are generally in agreement. The EBSD-measured Θ = 0.11°/μm for crystal A decently agrees with the calculated rotation rate of 0.16°/μm. However, crystal B's EBSD-measured Θ = 0.29°/μm does not agree that well with the calculated rotation rate of 0.73°/μm, but does agree with the SADP-measured rotation rate of 0.69°/μm. Measuring rotation rate with EBSD requires less sample preparation and hence yields more reliable values, but the value is mostly valid near sample surface at <100 nm depth [18]. Due to the higher rotation rate and hence greater density, the dislocations near the surface of crystal B are indistinguishable at the given TEM magnification due to interacting strain fields. SADP-measured rotation rate is measured with a 150 nm aperture positioned at the crystal center, below the indistinguishable layer. Since only the uppermost dislocations were discounted from the calculated rotation rate, it is reasonable that the SADP-measured and calculated rotation rates should be in better agreement. The discrepancy between EBSD-measured and SADP-measured rotation rates implies the discounted uppermost layer has partly relaxed the stresses that produce the rotation. This could

Table 2
Burgers vector component along $\overrightarrow{GD}$ (b_1) for both crystal samples for each dislocation type in Sb_2S_3.

Dislocation	Crystal A	Crystal B
$^1/_2[100]$	2.19 Å	1.79 Å
$^1/_4[102]$	0.33 Å	0.87 Å
$^1/_4[\bar{1}02]$	0.76 Å	1.23 Å

be attributed to the polishing of the crystal surface during sample preparation. Overall, the measured rotation rates can be almost completely explained by the presence of dislocations.

Crystal rotation rate must include the contribution of both plastic rotation from dislocations and elastic rotation. Nye created a generalized description of rotation rate by defining a curvature tensor, $\kappa_{ij} = \partial\theta_i/\partial x_j$, relating a rotation, θ_i, over some distance, x_j [8]. In this definition, the rotation rate, Θ, is a single off-diagonal component of κ_{ij}. Nye then related κ_{ij} to the dislocation density, α_{ij}, which was further connected to elastic strain gradients, $\varepsilon_{ikl}\partial\varepsilon_{lj}/\partial x_k$, by Kröner [9] in Eq. (1), where ε_{ikl} is the permutation symbol and δ_{ij} is the Kronecker delta.

$$k_{ij} = {\alpha_{ij}}^T - \frac{1}{2}tr(\alpha_{ij})\delta_{ij} + \varepsilon_{ikl}\frac{\partial\varepsilon_{lj}}{\partial x_k} \tag{1}$$

Elastic strain can be difficult to quantify accurately, especially with TEM since sample preparation requires significant thinning, yet the implications can be considered. If we define $\overrightarrow{GD}$, $\overrightarrow{ND}$, $\overrightarrow{B}$ as 1, -2, and 3 respectively, then $\Theta = \kappa_{31}$ and we can simplify Eq. (1) into (2). This shows how the rotation rate of the crystal may be elastically compensated. Given RLS crystals can be grown indefinitely long, it is unlikely there are any significant strain gradients along $\overrightarrow{GD}$ far away from the crystal growth front. This means the first elastic term is likely negligible and most of the elastic rotation rate is contributed by depth gradients of normal strain. As the crystal cools below the glass transition temperature, stresses will develop from differences in thermal expansion between the glass and crystal and the shape of the temperature depth profile. The relative nonuniformity between these two thermal effects will determine $\partial\varepsilon_{11}/\partial x_2$. Given that calculated rotation rates overpredict measured values (Table 1.), the elastic rotation may counteract the plastic rotation [1]. Despite this, elastic strain gradients can only be so large before dislocations start to nucleate and are usually small compared to lattice rotation rates from dislocations.

$$\Theta = \kappa_{31} = \alpha_{13} + \frac{\partial\varepsilon_{21}}{\partial x_1} - \frac{\partial\varepsilon_{11}}{\partial x_2} \tag{2}$$

Nye's dislocation density tensor is defined as $\alpha_{ij} = b_i\rho_j$, where b_i is the i^{th} component of the Burgers vector and ρ_j is the dislocation density through a surface j. In the absence of strain gradients, Eq. (2) can be rearranged into Eq. (3). This indicates the geometrically necessary dislocation density is inversely proportional to the Burgers vector component. By normalizing by the rotation rate, Eq. (3) can be compared between different crystal growth conditions.

$$\frac{\rho_3}{\kappa_{31}} = \frac{1}{b_1} \tag{3}$$

The minimum of Eq. (3) of the three dislocations can be used to help determine the expected slip mechanism. b_1 has been tabulated for each dislocation for both crystal samples in Table 2. For crystal A, Eq. (3) is minimized for $^1/_2[100]$ dislocations, indicating the lowest required dislocation density to achieve a given rotation rate. For crystal B, it must be noted that Eq. (3) is only for geometrically necessary dislocations and not entirely indicative of dislocation energies. Crystal B has both $^1/_2[100]$ and $-^1/_4[\bar{1}02]$ dislocations indicating the latter requires less energy per dislocation even though more are required for a given rotation rate. This type of analysis becomes more interesting when $\overrightarrow{GD}$= ⟨010⟩, where Eq. (3) approaches infinity. There are no slip mechanisms along ⟨010⟩, consequently the rotation rate has been noted near zero [1]. A more rigorous study would be required to better establish this relationship between rotation rate and Burgers vector components for all $\overrightarrow{GD}$.

We have confirmed dislocations as the source of lattice rotation, but there remain questions about the source of dislocations into the growing crystals. Geometrically similar transrotational crystals demonstrate the same type of rotation, but without dislocations [10,11]. Transrotational crystals are very thin, so the smaller volume significantly reduces the energy cost of elastic rotation. Other growth actuated deformations, such as curved ice growth [19], scrolled polymers [20], twisting in spherulites [21], and fractal and hierarchical structures [22,23] have been attributed to fields and stresses that develop near the growing crystal surface. Although these theories can explain the presence of dislocations of the same sign, they do not always account for how the dislocations are incorporated dynamically into the growing crystal. Dislocations could arise by homogenous (not likely due to large threshold shear stresses) or surface nucleation due to the presence of shear stresses [24], by autodefomation [4,5], or by a particle attachment mechanism [25,26]. A better understanding of how dislocations are introduced would help control lattice rotation in these crystals and other growth actuated deformations.

In conclusion, we have directly observed and characterized dislocations in Sb_2S_3 RLS crystals laser-fabricated in Sb-S-I glass as a model for establishing the source of lattice rotation in these crystal-in-glass metamaterial architectures. The rotation rates calculated from density and Burgers vectors of principal edge dislocations are in agreement with those experimentally measured by EBSD or SADP. Elastic contribution to lattice rotation, which is relatively small, could account for the overprediction of rotation rate by dislocations alone. Thus, a dislocation-based mechanism has been confirmed to explain the observation of lattice rotation in RLS crystals. This mechanism may also be applicable for other growth actuated deformations such as lattice distortions in widely studied spherulites and transrotational crystals in other systems.

Declaration of Competing Interest

The authors declare that they have no known competing financial interests or personal relationships that could have appeared to influence the work reported in this paper.

Acknowledgements

This work was supported by the Basic Energy Sciences Division of the Department of Energy for supporting this research under project DE-SC0005010. The authors would like to acknowledge B. Knorr for help with the laser control, S. McAnany for assistance with EBSD experiments, and M. Watanabe, R. Keyes, and J. Cline for assistance with TEM experiments.

References

[1] D. Savytskii, H. Jain, N. Tamura, V. Dierolf, Sci. Rep 6 (36449) (2016).
[2] D. Savytskii, C. Au-Yeung, V. Dierolf, N. Tamura, H. Jain, Cryst. Growth Des. 17 (4) (2017) 1735–1746.
[3] D. Savytskii, E. Musterman, V. Dierolf, H. Jain, Cryst. Growth Des. 19 (11) (2019) 6324–6330.
[4] A.G. Shtukenberg, Y.O Punin, E. Gunn, B. Kahr, Chem. Rev. 112 (2012) 1805–1838.
[5] A.G. Shtukenberg, Y.O Punin, A. Gujral, B. Kahr, Angew. Chem. Int. Edit. 53 (2014) 672–699.
[6] R.I. Barabash, G.E. Ice, F.J. Walker, J. Appl. Phys 93 (3) (2003) 1457–1463.
[7] J.M. Burgers, Proc. Phys. Soc. 52 (1940) 23–33.
[8] J.F. Nye, Acta Metall, Mater 1 (2) (1953) 152–162.

[9] E. Kröner, Zeitschrift für Physik 142 (1955) 463–475.
[10] V. Yu Kolosov, A.R. Thölén, Acta Mater 48 (8) (2000) 1829–1840.
[11] B.J. Kooi, J.Th.M De Hosson, J. Appl. Phys. 95 (9) (2004) 4714–4721.
[12] P. Gupta, A. Stone, N. Woodward, V. Dierolf, H. Jain, Opt. Express 1 (4) (2011) 652.
[13] A. Kyono, M. Kimata, M. Matsuhisa, Y. Miyashita, K. Okamoto, Phys. Chem. Miner. 29 (4) (2002) 254–260.
[14] EDAX OIM Analysis Page. https://www.edax.com/products/ebsd/oim-analysis.
[15] A.A. Sokol, V.M. Kosevich, A.G. Bagmut, Springer, Boston, MA, 1986, pp. 322–331. Growth of Crystals.
[16] Y. Zhang, S. Wang, C. Esling, J.S. Lecomte, C. Scuman, X. Zhao, L. Zuo, J. Appl. Crystallogr 44 (2001) 1164–1168.
[17] V. Volterra, Annales Scientifiques de, l'Ecole Normale Supérieure, Sér. 3 (24) (1907) 401–517.
[18] W. Wisniewski, S. Saager, A. Böbenroth, C. Rüssel, Ultramicroscopy 173 (2017) 1–9.
[19] C.A. Knight, J. Appl. Phys 33 (5) (1962) 1808–1815.
[20] B. Lots, S.Z.D. Cheng, Polymer 46 (2005) 577–610.
[21] J.M. Shultz, Polymer 44 (2003) 433–441.
[22] S. Busch, H. Dolhain, A. Duchesne, S. Heinz, O. Hochrein, F. Laeri, O. Podebrad, U. Vietze, T. Weiland, R. Kneip, Eur. J. Inorg. Chem. (1999) 1643–1653.
[23] G.Y. Chen, B. Dneg, G.B. Cai, T.K. Zhang, W.F. Dong, W.X. Zhang, A.W. Xu, J. Phys. Chem. C (2008) 672–679.
[24] D. Hull, D.J. Bacon, Introduction to Dislocations, Butterworth-Heinemann, Oxford, 2001.
[25] R.L. Penn, J.F. Banfield, Science 281 (1998) 969–971.
[26] J.J. De Yoreo, P.U.P.A. Gilbert, N.A.J.M. Sommerdijk, R.L. Penn, S. Whitelam, D. Joester, H. Zhang, J.D. Rimer, A. Navrotsky, J.F. Banfield, A.F. Wallace, F.M. Michel, F.C. Meldrum, H. Cölfen, P.M. Dove, Science 349 (2015).